SUBMILLIMETER QUASI-PERIODIC OSCILLATIONS
IN MAGNETICALLY CHOKED ACCRETION FLOW MODELS OF SGRA*

Roman V. Shcherbakov[1,2,3], Jonathan C. McKinney[2,4]

Draft version August 12, 2013

ABSTRACT

High-frequency quasi-periodic oscillations (QPOs) appear in general-relativistic magnetohydrodynamic simulations of magnetically choked accretion flows around rapidly rotating black holes (BHs). We perform polarized radiative transfer calculations with ASTRORAY code to explore the manifestations of these QPOs for SgrA*. We construct a simulation-based model of a radiatively inefficient accretion flow and find model parameters by fitting the mean polarized source spectrum. The simulated QPOs have a total sub-mm flux amplitude up to 5% and a linearly polarized flux amplitude up to 2%. The oscillations reach high levels of significance $10-30\sigma$ and high quality factors $Q \approx 5$. The oscillation period $T \approx 100M \approx 35$ min corresponds to the rotation period of the BH magnetosphere that produces a trailing spiral in resolved disk images. The total flux signal is significant over noise for all tested frequencies 87 GHz, 230 GHz, and 857 GHz and inclination angles $10°$, $37°$, and $80°$. The non-detection in the 230 GHz Sub-Millimeter Array light curve is consistent with a low signal level and a low sampling rate. The presence of sub-mm QPOs in SgrA* will be better tested with the Atacama Large Millimeter Array.

Subject headings: accretion, accretion disks — black hole physics — Galaxy: center — instabilities — magnetohydrodynamics (MHD) — radiative transfer

1. INTRODUCTION

Quasi-periodic oscillations (QPOs) in the emission from black hole (BH) accretion disks and jets are found in systems with both stellar mass BHs (Remillard & McClintock 2006) and supermassive BHs (SMBHs) (Gierliński et al. 2008; Reis et al. 2012). The high-frequency QPOs (HFQPOs) with a period T about the orbital period at the innermost stable circular orbit (ISCO) potentially probe the region close to the event horizon, offering a chance to test accretion and jet theories in the strong gravity regime. There have been multiple claims of the HFQPOs from the SMBH SgrA* in the Milky Way center, which then provides a unique opportunity to study the HFQPOs up-close. Henceforth, we set the speed of light and gravitational constant to unity ($c = 1$ and $G = 1$), such that $1M = 21$ s for SgrA* with the BH mass $M_{\rm BH} = 4.3 \times 10^6 M_\odot$ (Ghez et al. 2008; Gillessen et al. 2009). A HFQPO period commonly claimed for SgrA* is $T = 17$min $= 48M$. This was suggested in the K band during a flare (Genzel et al. 2003), in 7 mm data by Yusef-Zadeh et al. (2011), and in images obtained with very long baseline interferometry (VLBI) by Miyoshi et al. (2011). Periods of $T = 28$min $= 79M$ (Genzel et al. 2003), $T = 23$min $= 65M$, and $T = 45$min $= 127M$ (Trippe et al. 2007; Hamaus et al. 2009) were reported in the IR observations of flares. However, Do et al. (2009) analyzed a long K band light curve and found no statistically significant power spectrum density excess. A statistically significant longer period of $T = 2.5-3$hrs $\approx 470M$ was reported by Mauerhan et al. (2005) in 3 mm data. Miyoshi et al. (2011) claimed a range of periods from 17 min

to 56 min due to the spirals with multiple arms, but did not compute significance.

Physical origins of the HFQPOs are highly debated. Models are often based on an ISCO orbital frequency, an epicyclic frequency, and frequencies of various pressure and gravity modes (e.g., Kato 2001, 2004; Remillard & McClintock 2006; Wagoner 2008). The underlying physics involves beat oscillations (van der Klis 2000), resonances between flow modes and normal frequencies in general relativity (GR) (Abramowicz & Kluźniak 2001), trapped oscillations (Nowak & Wagoner 1991), parametric resonances (Abramowicz et al. 2003), and disk magnetospheric oscillations (Li & Narayan 2004).

The analytic methods were followed by blind QPO searches in magnetohydrodynamic (MHD) simulations. Non-GR 2D MHD simulations exhibited spiral patterns of Rossby waves detectable in simulated light curves (Tagger & Melia 2006; Falanga et al. 2007). Non-GR 3D MHD simulations of thick accretion disks by Chan et al. (2009) developed the QPOs with a period $T = 39M$ [5] in a simulated X-ray light curve. The 3D GRMHD simulations and radiative transfer by Schnittman et al. (2006) revealed weak transient QPOs. Similar simulations and radiative transfer by Dolence et al. (2009, 2012) showed a spiral structure producing oscillations with periods $T = 6-9$min $= 17-25M$ in simulated NIR and X-ray light curves. The GRMHD simulations of tilted disks produce tentative QPOs in dynamical quantities with $T \approx 170M = 1$ hr (Henisey et al. 2012).

Such MHD simulations start with a weak magnetic field, which is amplified by the magneto-rotational instability (MRI) that generates incoherent turbulence. However, when magnetized gas falls onto a BH, the disk becomes saturated with more magnetic flux than the MRI can generate (McKinney et al. 2012). The 3D GRMHD simulations of radiatively inefficient accretion flows (RIAFs, as applicable

roman@astro.umd.edu

[1] http://astroman.org
Department of Astronomy, University of Maryland, College Park, MD 20742, USA
[2] Joint Space Science Institute, University of Maryland, College Park MD 20742, USA
[3] Hubble Fellow
[4] Physics Department, University of Maryland, College Park, MD 20742-4111, USA

[5] We rescale reported periods to the current value of SgrA* BH mass.

to SgrA*) with ordered magnetic flux were performed by McKinney et al. (2012). The resultant magnetically choked accretion flow (MCAF) has a BH magnetosphere that significantly affects the sub-Keplerian equatorial inflow. The simulations showed high-quality disk-BH magnetospheric QPOs in dynamical quantities with an $m = 1$ (one-arm) toroidal mode and a rotating inflow pattern in the equatorial plane.

We quantify the QPO signal and its statistical significance in simulated SgrA* light curves based on the GRMHD simulations of MCAFs. We do a targeted search for the known QPO period $T \approx 100M$. In Section 2 we describe the 3D GRMHD simulations and the application to SgrA*. We perform GR polarized radiative transfer calculations with AS-TRORAY code, fit the SgrA* mean polarized spectrum, and find the best-fitting model parameters. In Section 3 we describe timing analysis. We study the light curves of the best-fitting model viewed at different inclination angles θ. We find statistically significant QPOs in total and some linearly polarized (LP) fluxes. We image a correspondent equatorial plane spiral wave. In Section 4 we compare our simulated QPOs with previous work and discuss the observability in SgrA*.

2. SGRA* MODEL BASED ON GRMHD SIMULATIONS

2.1. *GRMHD Simulations*

The initial gas reservoir is a hydrostatic torus (Gammie et al. 2003), within which magnetic field loops are inserted. The MRI action on the initial field leads to MHD turbulent accretion that eventually causes magnetic flux to saturate near the BH (McKinney et al. 2012). We focus on a simulation with a dimensionless spin $a_* = 0.9375$, which is close to $a_* \approx 0.9$ favored in simulation-based modeling of the SgrA* spectrum and the emitting region size (Mościbrodzka et al. 2009; Dexter et al. 2010; Shcherbakov et al. 2012). The simulation is performed in spherical coordinates (r, θ, ϕ) with resolution $N_r \times N_\theta \times N_\phi = 272 \times 128 \times 256$. It reached a quasi-steady state by time $t = 8,000M$ and ran till $t = 28,000M$. In steady state near the BH event horizon, the sub-Keplerian inflow is balanced against the BH magnetosphere resulting in vertical compression of the disk.

The BH magnetosphere and disk exhibit the QPOs in dynamical quantities such as the magnetic field energy density. A toroidal wobbling mode with $m = 1$ is eminent in the jet polar region and disk plane. It was identified with pattern rotation of the BH magnetospheric region pierced by the infalling matter streams. The streams form due to magnetic Rayleigh-Taylor instabilities (e.g. Stone & Gardiner 2007). The pattern rotates with an angular frequency $\Omega_F \approx 0.2\Omega_H$, where $\Omega_H = a_*/(2r_H)$ is the BH angular frequency and $r_H = (1 + \sqrt{1-a_*^2})M$ is the horizon radius. The angular frequency Ω_F is close to the rotation frequency $\approx 0.27\Omega_H$ of the field lines attached to the BH at the equatorial plane in a paraboloidal magnetospheric solution (Blandford & Znajek 1977).

2.2. *SgrA* Accretion Flow Model*

We use this MCAF 3D GRMHD simulation to model the SgrA* accretion flow. We follow Shcherbakov et al. (2012) to define the electron temperature and extrapolate quantities to outer radii $r > 50M$. A power-law extension of density to $r > 50M$ is $n \propto r^{-\beta}$, while the proton temperature is continued as $T_p \propto r^{-1}$. The magnetic field strength is extended as $b \propto \sqrt{nT_p} \propto r^{(-1-\beta)/2}$ to preserve a constant local ratio of magnetic field energy to thermal energy. The slope β is found by

connecting the known density at $r = 3 \times 10^5 M$ to the density in the inner region (Shcherbakov & Baganoff 2010). Correct simultaneous evolution of the simulations and the radiation field is considered, despite the radiative transfer is conducted in post-processing.

We focus on the accretion disk as the source of SgrA* emission and will consider jet emission (e.g., Falcke et al. 2004) in future studies. The simulated matter density is artificial near the polar axis, because matter is injected there to avoid an exceedingly high local ratio of magnetic energy to rest-mass energy that is difficult for GRMHD codes to evolve. The injected material does not change flow dynamics because it is energetically negligible. Nevertheless, a small amount of hot matter in the polar region can shine brightly as revealed by Mościbrodzka et al. (2009). The matter densities are zeroed out in a bipolar cone with an opening angle $\theta = 26°$. If that artificial matter was not removed, then none of our models would be consistent with the observed image size at 230 GHz (Doeleman et al. 2008) and the observed polarized SgrA* spectrum.

The radiative transfer is performed with our ASTRORAY code (Shcherbakov & Huang 2011; Shcherbakov et al. 2012). We compute radiation over a quasi-steady simulation period between $t = 8,000M$ and $t = 28,000M$. Following the previous work, we fit the total flux of SgrA* at $87 - 857$ GHz, the LP fraction at 87 GHz, 230 GHz, and 345 GHz, and the circular polarization (CP) fraction at 230 GHz and 345 GHz. We vary the heating constant C, which determines the electron temperature T_e close to the BH, the accretion rate $\dot{M}$, and the inclination angle θ. Fitting the mean SgrA* spectrum with the mean simulated spectrum we reach $\chi^2/\text{dof} = 1.55$ for dof = 9, which is a better agreement than in our prior work based on weakly magnetized simulations (Penna et al. 2010; Shcherbakov et al. 2012). The correspondent values of parameters are $T_e = 3.2 \times 10^{10}$ K at $6M$ distance from the center, $\dot{M} = 1.0 \times 10^{-8} M_\odot \text{yr}^{-1}$, and $\theta = 37°$. We then perform a timing analysis of the light curves from a number of models.

3. TIMING ANALYSIS

3.1. *Oscillations in Light Curves and Images*

Let us first demonstrate the oscillations in the light curves. In Figure 1 we show the light curves at times $t = 25,500M - 26,100M$ for the best-fitting model with the inclination angle $\theta = 37°$. The light curves are computed for three frequencies with different optical depth: radiation at 87 GHz is optically thick, the optical depth at 230 GHz is about $\tau \sim 1$, while radiation is optically thin at 857 GHz. The total flux (top panel) shows regular oscillations with the amplitude $\Delta F \approx 0.05$ Jy at 87 GHz and $\Delta F \approx 0.15$ Jy at 230 GHz. Fluctuations at 857 GHz with the amplitude $\Delta F \approx 0.2$ Jy are less regular. The LP fraction fluctuates at 2% level at all three frequencies, which translates into the relative variations of up to 50% and the absolute LP flux variations $\Delta F \approx 0.06$ Jy. The LP and CP fractions and the electric vector position angle (EVPA) exhibit substantial variations over long timescales at 87 GHz. The variations of the EVPA at 230 GHz and 857 GHz are about $5° - 10°$. The CP fraction oscillates by 0.3% at 87 GHz and by 0.15% at the higher frequencies. The absolute CP flux variations are $\Delta F \approx 0.005$ Jy at 230 GHz.

In Figure 2 we show how the amplitude of oscillations depends on the inclination angle θ at 230 GHz. Shown are the light curves for the best-fitting inclination angle $\theta = 37°$, for almost face-on $\theta = 10°$, and for almost edge-on $\theta = 80°$.
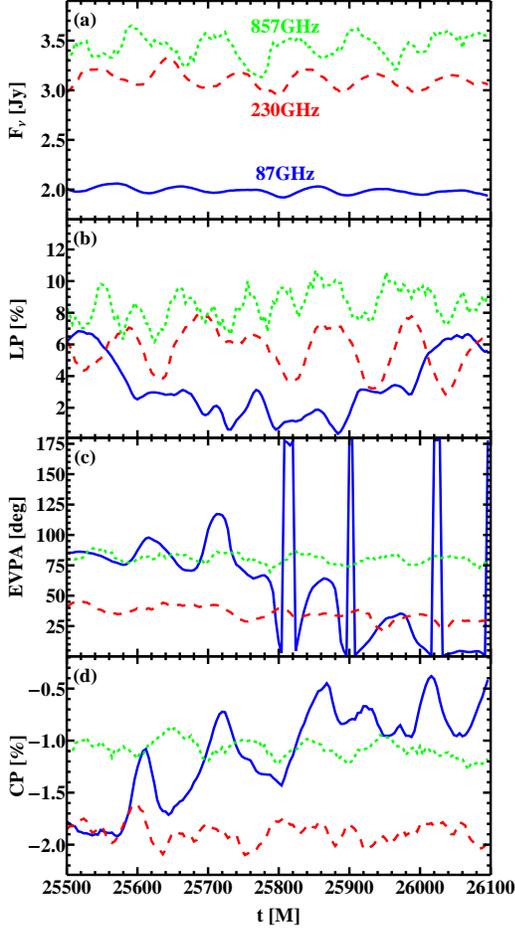
FIG. 1.— Polarized light curve fragments for the best-fitting model with the inclination angle $\theta = 37°$ at the optically thick 87 GHz (blue solid line), at 230 GHz (red dashed line) with the optical depth about unity, and at the optically thin 857 GHz (green dotted line).

FIG. 2.— Polarized light curve fragments at 230 GHz for the best-fitting T_e and $\dot{M}$ for several inclination angles θ: best-fitting $\theta = 37°$ (solid line), face-on $\theta = 10°$ (dashed line), and edge-on $\theta = 80°$ (dotted line).

The total flux exhibits the same oscillation amplitude $\Delta F \approx 0.15$ Jy independent of θ. The edge-on and the best-fitting cases produce comparable variations of the LP fraction, while cancelations of the polarized fluxes emitted across the flow lower both the mean and the fluctuation amplitude of the LP fraction in the face-on case. Correspondingly, the EVPA fluctuates dramatically in the face-on case. The CP fraction oscillates at 0.5% level in the edge-on case, while the other cases exhibit oscillation amplitude 0.15%.

The face-on accretion flow images with $\theta = 10°$ are shown in Figure 3: the time series of the total intensity images in the top row and of the LP intensity images in the bottom row. The total intensity images show a clear one-arm spiral rotating with a period $T \approx 100M$. The LP intensity spiral is spatially offset from the total intensity spiral, as the region of the brightest total intensity exhibits the strongest LP cancelations. The total intensity spiral looks similar to that in Dolence et al. (2012), despite different angular velocities. Note that we report the intensity images, while Dolence et al. (2012) showed the images of the dynamical quantities.

3.2. *Statistical Analysis*

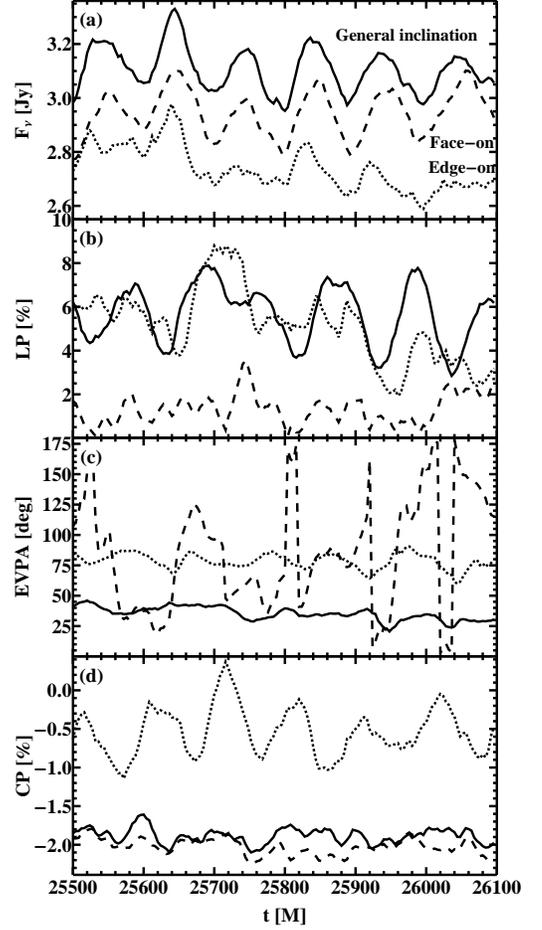Let us quantify significance of the QPOs. Following Papadakis & Lawrence (1993) we start with an autocovari-

ance

$$\hat{R}(k) = \frac{1}{N} \sum_{t=1\Delta t}^{N\Delta t - |k|} (x_t - \bar{x})(x_{t+|k|} - \bar{x}), \qquad (1)$$

where $k = 0, \pm 1\Delta t, ..., \pm (N-1)\Delta t$ and x_t is the sample of simulated fluxes normalized to have its mean $\bar{x}$ equal unity. Then we compute a periodogram

$$I(R) = \frac{\Delta t}{2\pi} \sum_{k=-(N-1)\Delta t}^{(N-1)\Delta t} \hat{R}(k) \cos \omega k, \quad -\frac{\pi}{\Delta t} \le \omega \le \frac{\pi}{\Delta t}. \qquad (2)$$

In our analysis $\Delta t = 4M$, which appears large enough to avoid aliasing at periods $T > 50M$. All periodograms are log-smoothed Papadakis & Lawrence (1993) to 0.08dex as a compromise between stronger random noise and larger smearing of the QPO peaks.

The determination of statistical significance of the QPOs involves comparison of the simulated periodogram with the random noise periodograms. We follow the procedure in Timmer & Koenig (1995) for random noise generation. We employ a log-smoothed to 3.0dex periodogram of the simulated light curve as the underlying non-QPO periodogram. This approximation produces a smooth curve comparable to fits of the non-QPO power spectrum with a power-law of a
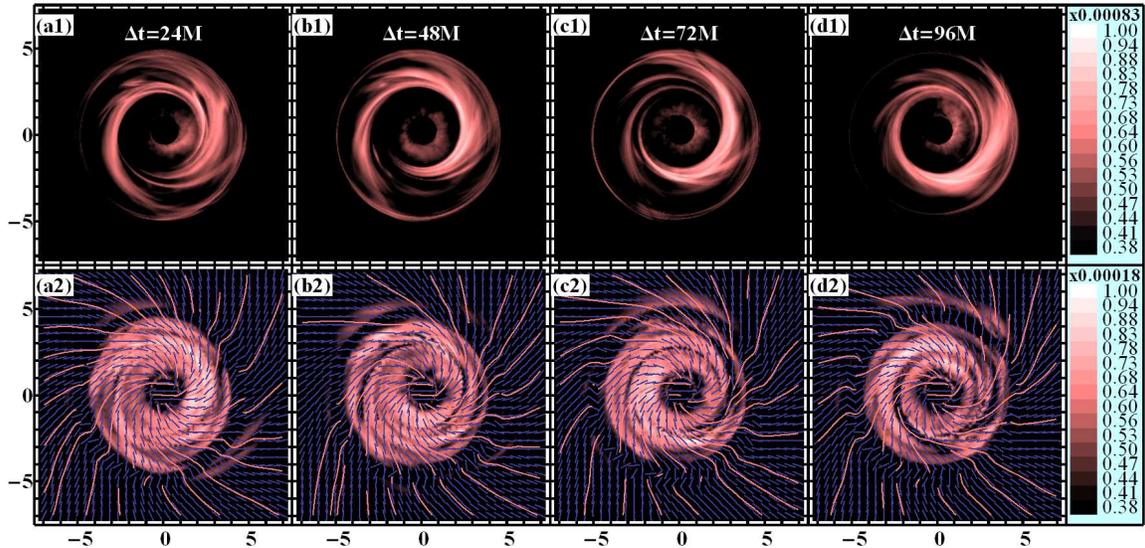
FIG. 3.— Images of a face-on disk at 230 GHz: the total intensity images (top row) and the LP intensity images (bottom row). Strokes indicate the EVPA direction. The rotating spiral pattern is clearly visible.

broken power-law. We draw the random noise Fourier transform from a normalized Gaussian distribution and perform the inverse Fourier transform to generate the noise light curves. We then compute noise autocovariances and periodograms. We find a 3σ significance curve based on $2,592$ random noise samples. We do not correct for the blind search, since the periodograms are binned, and we target the QPOs with a period $T \approx 100M$.

The periodograms with their 3σ significance curves are depicted in the top six panels of Figure 4 for several frequencies and inclination angles. The top curves in each panel are for almost face-on inclination $\theta = 10°$, the middle curves are for $\theta = 37°$, and the bottom curves are for almost edge-on $\theta = 80°$. We report the statistical significance levels and quality factors $Q = T_{QPO}/$FWHM. The total flux and the LP fraction periodograms exhibit peaks significant to $5 - 30\sigma$ with $Q = 2 - 5$ at the period $T \approx 100M$ for most studied frequencies and inclination angles. Our method allows for the maximum measurable quality of $Q = 8 - 11$. A face-on disk shows weaker QPOs, which are not significant at 857 GHz. The LP fraction oscillations are weak for a face-on disk for all frequencies due to random cancelations of the LP. The total flux and the LP fraction at 230 GHz show the strongest oscillations, which further encourages SgrA* observations at 1.3 mm wavelength. We also detect marginally significant LP fraction oscillations with a period $T = 1000M \approx 4$ hr. The bottom left panel of Figure 4 shows the analysis for the different approximations to the non-QPO periodogram: the power-law fit, the broken power-law fit, and the log-smoothed to 3.0dex source periodogram. The bottom right panel of Figure 4 shows the analysis for the different azimuthal viewing angles $\phi = 0$deg, $\phi = 120$deg, and $\phi = 240$deg. The QPO peaks in these six cases stay prominent despite the significance level (number of sigmas) varies by 50%. The significant QPO peaks among the cases presented in Figure 4 (top panels) stay significant, when we switch to the broken power-law fits to the non-QPO periodograms.

We characterize presence of the oscillations and stability of the oscillation period by a spectrogram in Figure 5. The spectrogram indicates that most of the time oscillations with

a period $T = 90 - 100M$ are present. However, no oscillations occur around time $t = 22,000M$, when the accretion rate peaks due to weaker magnetic field.

4. DISCUSSION AND CONCLUSIONS

4.1. *Summary and Comparison to Previous Work*

Here we report the QPOs in the simulated SgrA* light curves for models based on the state-of-the-art 3D GRMHD simulations of the magnetically choked RIAFs. The minimization procedure produces a fit with $\chi^2/$dof $= 1.55$ for dof $= 9$ to the mean polarized sub-mm source spectrum. The correspondent simulated total flux light curve shows regular oscillations with the period $T \approx 100M \approx 35$ min and the amplitude $\Delta F \approx 0.15$ Jy at 230 GHz. Less regular fluctuations with $\Delta F \approx 0.2$ Jy are seen at 857 GHz. Weaker oscillations with $\Delta F \approx 0.05$ Jy are seen at 87 GHz, which probes the optically thick emission from $\sim 10M$ radius. The LP fraction exhibits periodic modulations at 50% relative level, but the absolute LP flux amplitude is only about $\Delta F_{LP} \approx 0.06$ Jy. The QPOs are significant above 3σ in the total flux light curves for all tested inclination angles $10°$, $37°$, and $80°$ and frequencies 87 GHz, 230 GHz, and 857 GHz, while the LP fraction shows less prominent QPOs at 87 GHz and in a face-on case.

Our main $T \approx 35$ min period is longer than the claimed SgrA* observed period $17 - 20$ min, while the simulated periods $T = 6 - 9$ min in Dolence et al. (2012) are shorter. Their simulation has the same BH spin $a_* = 0.9375$ as does our simulation, but the simulation by Dolence et al. (2012) reaches a relatively weak BH horizon magnetic flux and produces a thinner disk with height-to-radius ratio of $H/R \sim 0.2$. The resultant MRI-dominated accretion flow has a Keplerian rotation and shorter QPO periods. They did not identify their QPO mechanism, although they noted their turbulence is unresolved (Shiokawa et al. 2012) and this might lead to artificial QPOs (Henisey et al. 2009). Our MCAF model has a sub-Keplerian rotation and the QPOs driven by the interaction of the disk with the rotating BH magnetosphere (Li & Narayan 2004) that leads to longer periods. Our relatively thick disk with $H/R \sim 0.6$ is expected for a RIAF, and our simulations resolve well the disk turbulence (McKinney et al. 2012) sug-
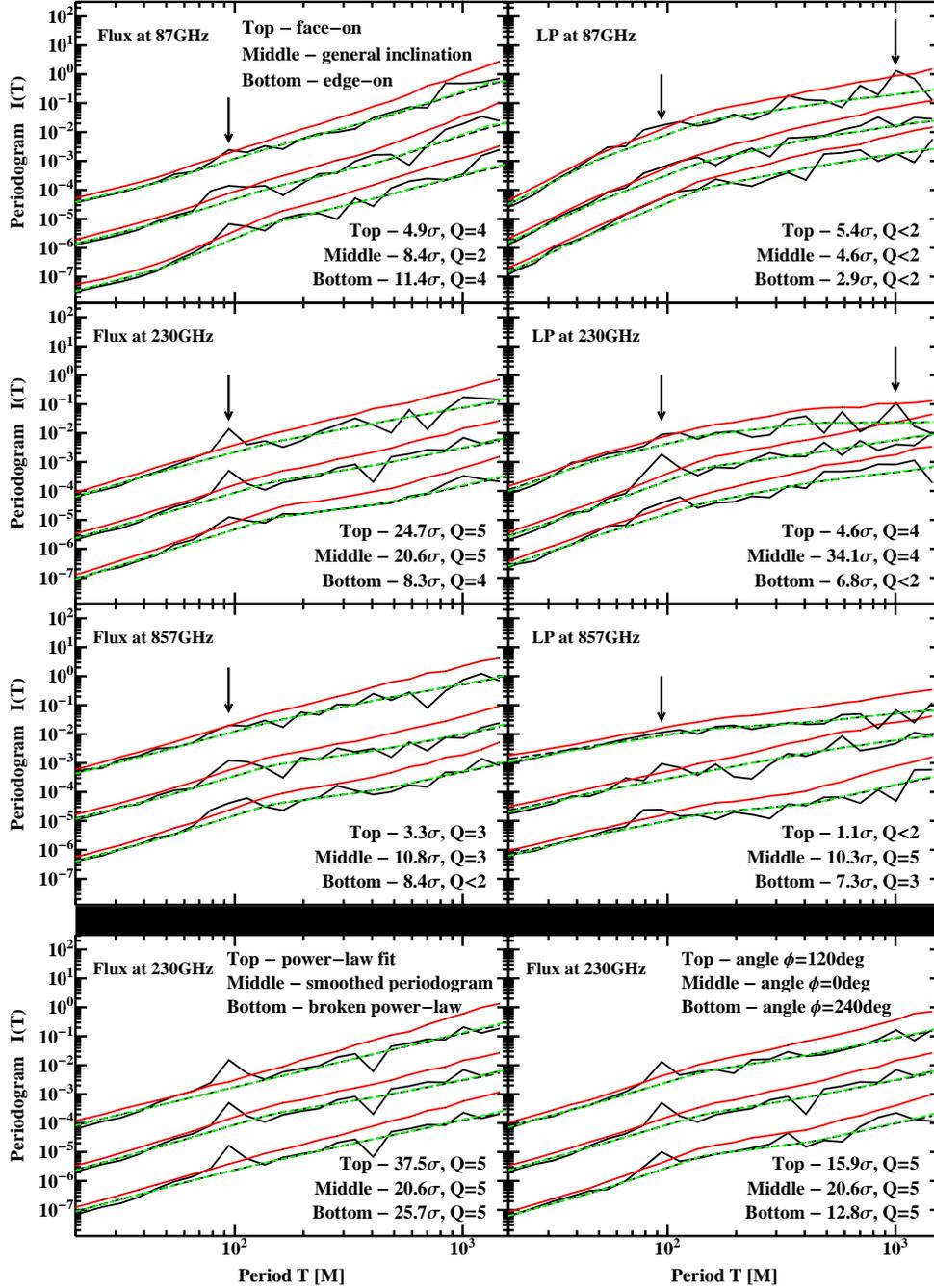
FIG. 4.— Periodograms of the total flux and the LP fraction light curves for the frequencies 87 GHz, 230 GHz, and 857 GHz and the inclination angles $\theta = 10°$ (top curves on top six panels), $\theta = 37°$ (middles curves), and $\theta = 80°$ (bottom curves), while T_e and $\dot{M}$ are fixed at their best-fitting values: simulated periodograms (black/dark solid lines), 3σ significance curves (red/light solid lines), log-smoothed to 3.0dex source periodograms (black/dark dashed lines), and geometric means of random noise periodograms (green/light dashed lines). The top six panels employ the log-smoothed to 3.0dex source periodogram as the underlying non-QPO periodogram and the azimuthal viewing angle $\phi = 0$deg. The bottom left panel shows the results for the different approximations of the non-QPO periodogram. The bottom right panel shows the results for the different azimuthal viewing angles.

gesting the QPOs are robust. Based upon these works, SgrA* QPOs might be explained by $a_* = 0.9375$ with an intermediate gas rotation rate, magnetization, or H/R.

Flow cooling, whose marginal importance for SgrA* was suggested by Drappeau et al. (2013), can self-consistently choose the disk thickness H/R in simulations. In MCAFs, the steady-state BH horizon magnetic flux has a positive correlation with H/R (McKinney et al. 2012), so cooling can lead to more Keplerian rotation and a weaker magnetosphere, and then the QPO period from MCAFs could be comparable to

claimed for SgrA*.

4.2. Observing QPOs in SgrA*

We showed that the QPOs, though highly significant, have a maximum sub-mm amplitude of 5% or $\Delta F \sim 0.15$ Jy. Low sensitivity and low sampling rate of current sub-mm instruments might prohibit observational detection of such oscillations (Marrone 2006). The SMA achieves 5% accuracy and samples every 10 min at 1.3 mm with a correspondent 20 min Nyquist period (Marrone et al. 2008). A weak signal with
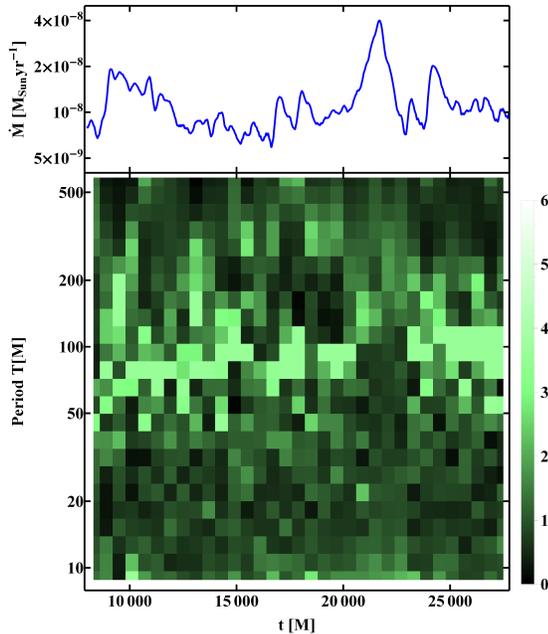
FIG. 5.— Accretion rate dependence on time $\dot{M}(t)$ (top) and normalized spectrogram of the total flux light curve (bottom) for the simulation intervals with $\Delta t = 600M$. The normalized spectrogram shows ratios of the log-smoothed to 0.08dex periodograms over the log-smoothed to 3.0dex periodograms. The higher ratio and the lighter color indicate the QPOs.

$T \sim 30$ min period is readily masked by aliasing and noise in the SMA data. The total flux QPO amplitude $\Delta F \approx 0.15$ Jy

is larger than the LP flux amplitude $\Delta F \approx 0.06$ Jy. However, the observational error of the total flux can also be larger. The SMA measures the LP flux to the leakage level of $\sim 0.3\% = 9$ mJy, while the total flux is measured to $\sim 0.7\% = 20$ mJy due to calibration uncertainties (Marrone et al. 2007). Then it is about equally difficult to detect the total flux oscillations and the LP flux oscillations.

The ALMA gives more hope in detecting SgrA* sub-mm QPOs. It covers a wide frequency range $84 - 720$ GHz, has a collecting area of $\sim 7 \times 10^3 \mathrm{m}^2$ about 30 times that of the SMA, and can sample every few minutes (Brown et al. 2004). The ALMA observations of SgrA* will have a flux error under 0.05 Jy, which is enough to reveal the predicted oscillations were they present on an observation night. As our modeling indicates, the QPOs are absent when the magnetic field is weak due to destruction by magnetic field reversals. The future implementation of the Event Horizon Telescope may allow to measure the QPOs in the source size variations (Doeleman et al. 2009). The anticipated brighter state of SgrA* (Mościbrodzka et al. 2012) after the cloud infall may alter our predictions: at a constant ν the flux increase is compensated by the lower fractional level of the QPOs due to the higher optical depth.

REFERENCES

Abramowicz, M. A., Karas, V., Kluzniak, W., Lee, W. H., & Rebusco, P. 2003, PASJ, 55, 467
Abramowicz, M. A., & Kluźniak, W. 2001, A&A, 374, L19
Blandford, R. D., & Znajek, R. L. 1977, MNRAS, 179, 433
Brown, R. L., Wild, W., & Cunningham, C. 2004, Advances in Space Research, 34, 555
Chan, C.-k., Liu, S., Fryer, C. L., Psaltis, D., Özel, F., Rockefeller, G., & Melia, F. 2009, ApJ, 701, 521
Dexter, J., Agol, E., Fragile, P. C., & McKinney, J. C. 2010, ApJ, 717, 1092
Do, T., Ghez, A. M., Morris, M. R., Yelda, S., Meyer, L., Lu, J. R., Hornstein, S. D., & Matthews, K. 2009, ApJ, 691, 1021
Doeleman, S. S., Fish, V. L., Broderick, A. E., Loeb, A., & Rogers, A. E. E. 2009, ApJ, 695, 59
Doeleman, S. S., et al. 2008, Nature, 455, 78
Dolence, J. C., Gammie, C. F., Mościbrodzka, M., & Leung, P. K. 2009, ApJS, 184, 387
Dolence, J. C., Gammie, C. F., Shiokawa, H., & Noble, S. C. 2012, ApJ, 746, L10
Drappeau, S., Dibi, S., Dexter, J., Markoff, S., & Fragile, P. C. 2013, MNRAS, 431, 2872
Falanga, M., Melia, F., Tagger, M., Goldwurm, A., & Bélanger, G. 2007, ApJ, 662, L15
Falcke, H., Körding, E., & Markoff, S. 2004, A&A, 414, 895
Gammie, C. F., McKinney, J. C., & Tóth, G. 2003, ApJ, 589, 444
Genzel, R., Schödel, R., Ott, T., Eckart, A., Alexander, T., Lacombe, F., Rouan, D., & Aschenbach, B. 2003, Nature, 425, 934
Ghez, A. M., et al. 2008, ApJ, 689, 1044
Gierliński, M., Middleton, M., Ward, M., & Done, C. 2008, Nature, 455, 369
Gillessen, S., Eisenhauer, F., Trippe, S., Alexander, T., Genzel, R., Martins, F., & Ott, T. 2009, ApJ, 692, 1075
Hamaus, N., Paumard, T., Müller, T., Gillessen, S., Eisenhauer, F., Trippe, S., & Genzel, R. 2009, ApJ, 692, 902
Henisey, K. B., Blaes, O. M., & Fragile, P. C. 2012, ApJ, 761, 18
Henisey, K. B., Blaes, O. M., Fragile, P. C., & Ferreira, B. T. 2009, ApJ, 706, 705
Kato, S. 2001, PASJ, 53, 1

Kato, Y. 2004, PASJ, 56, 931
Li, L.-X., & Narayan, R. 2004, ApJ, 601, 414
Marrone, D. P. 2006, PhD thesis, Harvard University
Marrone, D. P., Moran, J. M., Zhao, J.-H., & Rao, R. 2007, ApJ, 654, L57
Marrone, D. P., et al. 2008, ApJ, 682, 373
Mauerhan, J. C., Morris, M., Walter, F., & Baganoff, F. K. 2005, ApJ, 623, L25
McKinney, J. C., Tchekhovskoy, A., & Blandford, R. D. 2012, MNRAS, 423, 3083
Miyoshi, M., Shen, Z.-Q., Oyama, T., Takahashi, R., & Kato, Y. 2011, PASJ, 63, 1093
Mościbrodzka, M., Gammie, C. F., Dolence, J. C., Shiokawa, H., & Leung, P. K. 2009, ApJ, 706, 497
Mościbrodzka, M., Shiokawa, H., Gammie, C. F., & Dolence, J. C. 2012, ApJ, 752, L1
Nowak, M. A., & Wagoner, R. V. 1991, ApJ, 378, 656
Papadakis, I. E., & Lawrence, A. 1993, MNRAS, 261, 612
Penna, R. F., McKinney, J. C., Narayan, R., Tchekhovskoy, A., Shafee, R., & McClintock, J. E. 2010, MNRAS, 408, 752
Reis, R. C., Miller, J. M., Reynolds, M. T., Gültekin, K., Maitra, D., King, A. L., & Strohmayer, T. E. 2012, Science, 337, 949
Remillard, R. A., & McClintock, J. E. 2006, Ann. Rev. Astron. Astr., 44, 49
Schnittman, J. D., Krolik, J. H., & Hawley, J. F. 2006, ApJ, 651, 1031
Shcherbakov, R. V., & Baganoff, F. K. 2010, ApJ, 716, 504
Shcherbakov, R. V., & Huang, L. 2011, MNRAS, 410, 1052
Shcherbakov, R. V., Penna, R. F., & McKinney, J. C. 2012, ApJ, 755, 133
Shiokawa, H., Dolence, J. C., Gammie, C. F., & Noble, S. C. 2012, ApJ, 744, 187
Stone, J. M., & Gardiner, T. 2007, ApJ, 671, 1726
Tagger, M., & Melia, F. 2006, ApJ, 636, L33
Timmer, J., & Koenig, M. 1995, A&A, 300, 707
Trippe, S., Paumard, T., Ott, T., Gillessen, S., Eisenhauer, F., Martins, F., & Genzel, R. 2007, MNRAS, 375, 764
van der Klis, M. 2000, ARA&A, 38, 717
Wagoner, R. V. 2008, New Astronomy Reviews, 51, 828

Yusef-Zadeh, F., Wardle, M., Miller-Jones, J. C. A., Roberts, D. A., Grosso,
N., & Porquet, D. 2011, ApJ, 729, 44